Electronic Supplementary Material (ESI) for Energy & Environmental Science.
This journal is © The Royal Society of Chemistry 2022

Supplementary Information

In-Situ Protonated-Phosphorus Interstitial Doping Induces Long-Lived Shallow Charge Trapping in Porous $C_{3-x}N_4$ Photocatalyst for Highly Efficient H_2 Generation

Wenchao Wang,[a] Lili Du,[ae] Ruiqin Xia,[a] Runhui Liang,[a] Tao Zhou,[a] Hung Kay Lee,[d] Zhiping Yan,[a] Hao Luo,[a] Congxiao Shang,[a] David Lee Phillips,[ac] and Zhengxiao Guo*[ab]*

[a] Department of Chemistry and HKU-CAS Joint Laboratory on New Materials, The University of Hong Kong, Hong Kong SAR, PR China.

[b] Zhejiang Institute of Research and Innovation, The University of Hong Kong, Hangzhou 311305, PR China.

[c] Guangdong-Hong Kong-Macao Joint Laboratory of Optoelectronic and Magnetic Functional, Hong Kong SAR, PR China.

[d] Department of Chemistry, The Chinese University of Hong Kong, Shatin, New Territories, Hong Kong SAR, PR China.

[e] School of Life Science, Jiangsu University, Zhenjiang 212013, PR China.

* Corresponding authors: zxguo@hku.hk (Z. X. Guo); phillips@hku.hk (D. L. Phillips)

Table of Contents

Experimental Procedures

Materials

Urea (AR 99%, Aladdin), red phosphorus (AR 98.5%, Aladdin), triethanolamine (SigmaAldrich), $H_2PtCl_6 \cdot 6H_2O$ (SigmaAldrich). These chemical reagents were used without further purification.

Synthesis of bulk g-C_3N_4

Conventional thermal-polymerization method was employed to synthesize bulk g-C_3N_4.[1] Briefly, 10 g urea was heated at 823 K for 4 h, with a ramping rate of 10 K min^{-1}. The yellow bulk g-C_3N_4 was collected after natural cooling and ground into a powder for further use, denoted as BCN.

Synthesis of holey g-$C_{3-x}N_4$

Holey g-$C_{3-x}N_4$ (denoted as Ho@$C_{3-x}N_4$) was prepared by a facile thermal-exfoliation approach. Typically, BCN (0.5 g) was uniformly put into a rectangular crucible to make sure a good contact between BCN and air, followed by heating at 793 K for 2 h (few-layer), 4 h (ultrathin) and 6 h (holey), with a ramping rate of 5 K min^{-1}. The light-yellow to nearly white powder was obtained, respectively.

Fabrication of phosphorus-interstitial-doping in the Ho@$C_{3-x}N_4$

Phosphorus-interstitial-doping in Ho@$C_{3-x}N_4$ (denoted as Pi-Ho@$C_{3-x}N_4$) was synthesized by the thermal-evaporation method, where x represents the mass of commercial red phosphorus (50-250 mg). In detail, Ho@$C_{3-x}N_4$ (50 mg) and commercial red phosphorus (x mg) were uniformly placed in two crucibles, respectively, then heated to 723 K for 2 h in Argon with a ramping rate of 5 K min^{-1}.

Photocatalytic Measurements

Briefly, 10.0 mg photocatalyst and a certain amount of $H_2PtCl_6 \cdot 6H_2O$ (3.0 wt% Pt) were mixed and suspended into a 10 vol% triethanolamine aqueous solution under magnetic stirring and sonication in a 100 mL sealed Pyrex flask. Before photocatalytic tests, the above-mentioned suspension was purged via 15 min Argon bubbling to remove oxygen species (e.g., dissolved oxygen). A 300 W Xenon lamp (PerfectLight-SXE300) was equipped with a 400 nm cutoff filter was employed to trigger H_2 production. Evolved H_2 gas was reflected using gas chromatography (GC-7800 BEIJINGPURUI) with Argon as the carrier gas.

Quantum efficiency (QE) was carried out to investigate the solar-to-H_2 efficiency according to the following equation:[2]

$$QE=\frac{\text{number of evolved } H_2 \text{ molecules} \times 2}{\text{number of incident photons}}\times 100\%=\frac{2R_{H_2}N_A t_1}{EAt_2\lambda/hc}\times 100\%=\frac{6.6481\times 10^{-5}R_{H_2}}{EA\lambda}\times 100\%$$

where N_A is Avogadro's constant; t_1 and t_2 are the reaction times (h); E is the light intensity (31.2 mW/cm^2; A is the irradiation area, 0.64 cm^{-2}; λ is a single wavelength (420 nm); h is the Plank constant; and c is the speed of light (m/s); R_{H_2} is the H_2 evolution rate.

Internal quantum efficiency (IQE) was calculated under 400 nm irradiation by using the follow equation:[3]

$$IQE\ (\%)=\frac{n(H_2)\times 2}{n(\text{photons absorbed})}\times 100$$

where n(H_2) and n(photons) refer to the number of H_2 gas generated and the number of photons absorbed, respectively.

Characterizations

Morphological studies via scanning electron microscopy (SEM) and scanning transmission electronic microscopy (STEM) were collected by Hitachi S-4800 and Tecnai G2 20 S-TWIN instruments, respectively. Nitrogen adsorption-desorption experiments and UV-vis diffuse reflectance spectra (UV-vis DRS) were done by using Micromeritics Tristar Ⅱ 3020 and Shimadzu UV2450 instruments. X-ray diffraction (XRD) measurements were performed with a Rigacu Smartlab diffractometer. A Perkin-Elmer PHI 5000 instrument was employed to obtain X-ray photoelectron spectra (XPS). Electron paramagnetic resonance (EPR) was carried out by uisng Bruker EMX-EPR Spectrometer. Fourier transformation infrared (FTIR) spectra were obtained on an IRAffinity-1 spectrometer (Shimadzu). Steady-state photoluminescence (PL) spectroscopy measurements were recorded by F-7000 Hitachi instrument.

Photoelectrochemical Measurements

Photoelectrochemical measurements were acquired by a commercial electrochemical station (CHI 760E, Chen Hua Instrument Co., Ltd., China). For the working electrode preparation, a photocatalyst (2.0 mg), 1.0 mL of ethanol and 5.0 μL of 10% Nafion solution were mixed together, followed by spin-coating onto a substrate (ITO glass). A suspension was obtained by mixing the as-synthesized material with ethanol. The standard saturated calomel electrode (SCE) and platinum foil was used as the counter electrode and reference electrode, respectively. Na_2SO_4 (0.5 M) aqueous solution was used as the electrolyte. Different from the photocatalytic activity measurement, no Pt nanoparticles were added in the photoelectrochemical tests.

fs-TAS and ns-TAS Setup

fs-TAS measurements were collected with a femtosecond Ti/Sapphire regenerative amplifier laser system (Spitfire-Pro, Spectra-Physics Company), and an automated data acquisition transient absorption spectrometer (Ultrafast, Helios) was used to record the transient absorption spectra of the photocatalysts. The amplifier produced a 150 fs pulse at 800 nm (repetition rate at 1 kHz, average output energy was 2.5 W). In our experiments, the pump laser (400 nm) was obtained from the second harmonic generated from the 800 nm output from the Spitfire amplifier (approximately 95.0 % of the amplified output). The probe pulse (continuum white-light spectrum, 420 to 780 nm) was generated using the remaining 5.0 % of the amplified 800 nm output. Additionally, ns-TAS spectra were collected from a LP-920 laser system (Edinburgh Instruments). The Xenon lamp was the probe light source (450 W, model Xe900), which traversed the sample cell and the signal was recorded by an array detector (absorption mode) and a single detector (kinetic mode). The 355 nm pump laser pulse was generated by the third harmonic output of an Nd: YAG laser. For the fs-TAS and the ns-TAS experiments, all of the as-prepared catalysts were dispersed in water.

DFT Simulations

Density functional theory / time-dependent density functional theory (DFT/TDDFT) calculations were used to examine the charge separation of as-prepared catalysts, and the calculations were performed using the Gaussian16 software suite installed in the high-performance computing cluster at the University of Hong Kong. The B3LYP functional with 6-31G(d) basis set with the solvation model of Polarizable Continuum Model (PCM) in water was used for the geometry optimization. The CAM-B3LYP functional was used for the TDDFT calculations. The iso-surface of electron-hole distribution of the lowest excited states was plotted by Multiwfn. We analyzed the charge density difference (CDD), and electron-hole pair distance (ΔD) of the lowest excited states to characterize the charge separation performance. The formation energy and DOS was carried out using the Vienna Ab initio Simulation Package (VASP) in the framework of the DFT. The projector augmented wave (PAW) method was adopted to solve the Kohn-Sham equations,[4] and the generalized gradient approximation constructed by Perdew-Burke-Ernzerhof (GGA-PBE) was selected to describe the exchange-correlation functional.[5] The unitcell of g-C_3N_4 was first optimized, and then a 1 × 1 × 1 supercell was constructed to accommodate the P dopant, based on which the defect formation energy and electronic properties were calculated. The number of the k-points was set to be 2 × 2 × 1, along with a plane-wave cutoff energy of 480 eV, which made the accuracy within 1 meV per atom.

Band-Gap Calculation

Band-gap energy (E_g) was calculated by the Tauc plots, following the Kubelka-Munk equation:[6]

$$(\alpha h\upsilon)^2 = A(h\upsilon - E_g)$$

where α and h are the absorption coefficient and Planck's constant, υ and E_g the light frequency and band-gap energy, respectively.

Results and Discussion

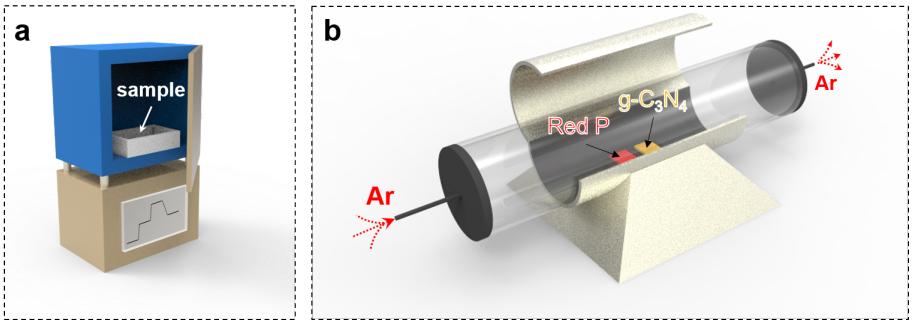

Fig. S1 (a) Thermal polycondensation and exfoliation system in air (b) thermal doping system under inert gas (Ar) protection.

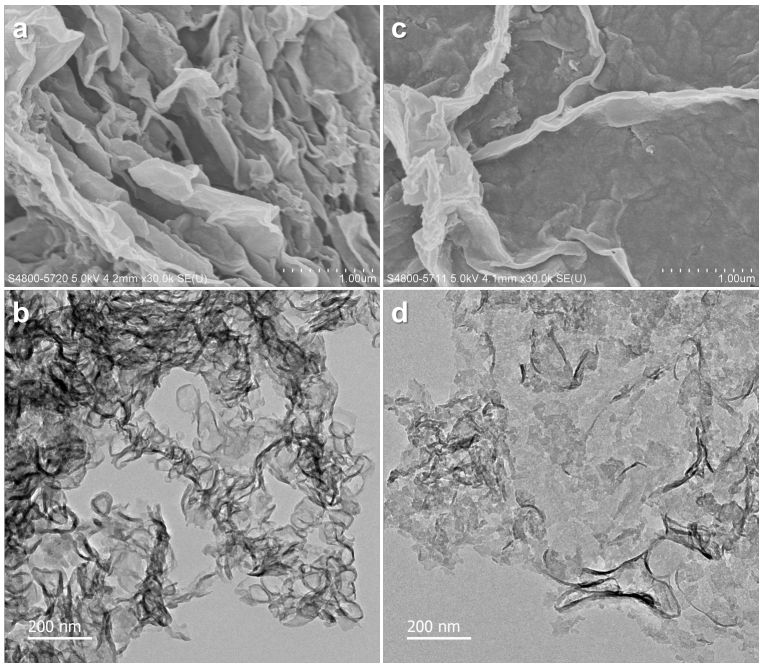

Fig. S2 SEM and STEM images of (a,b) FCN and (c,d) UCN, respectively.

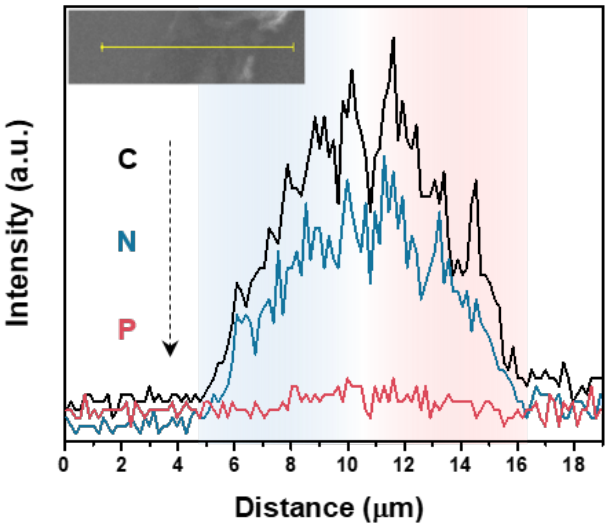

Fig. S3 EDX elements linear distribution of Pi-Ho@$C_{3-x}N_4$ sample.

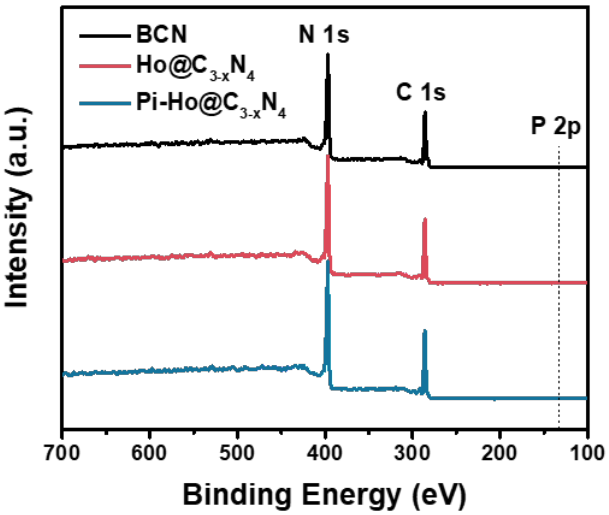

Fig. S4 XPS wide spectra of BCN, Ho@$C_{3-x}N_4$ and Pi-Ho@$C_{3-x}N_4$, respectively.

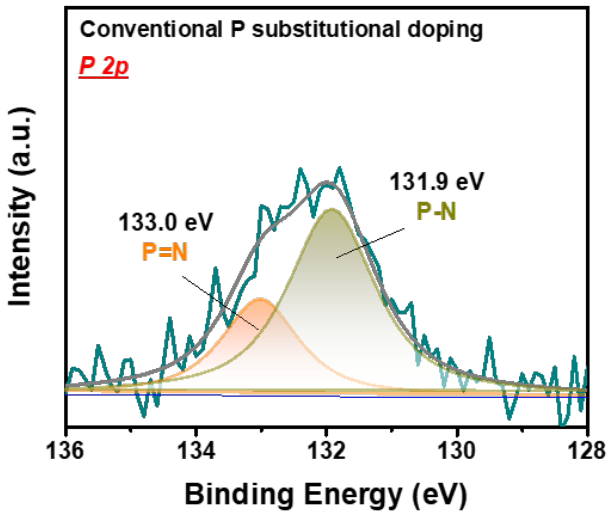

Fig. S5 High resolution XPS spectra for P 2p of phosphorus substitutional doped BCN.

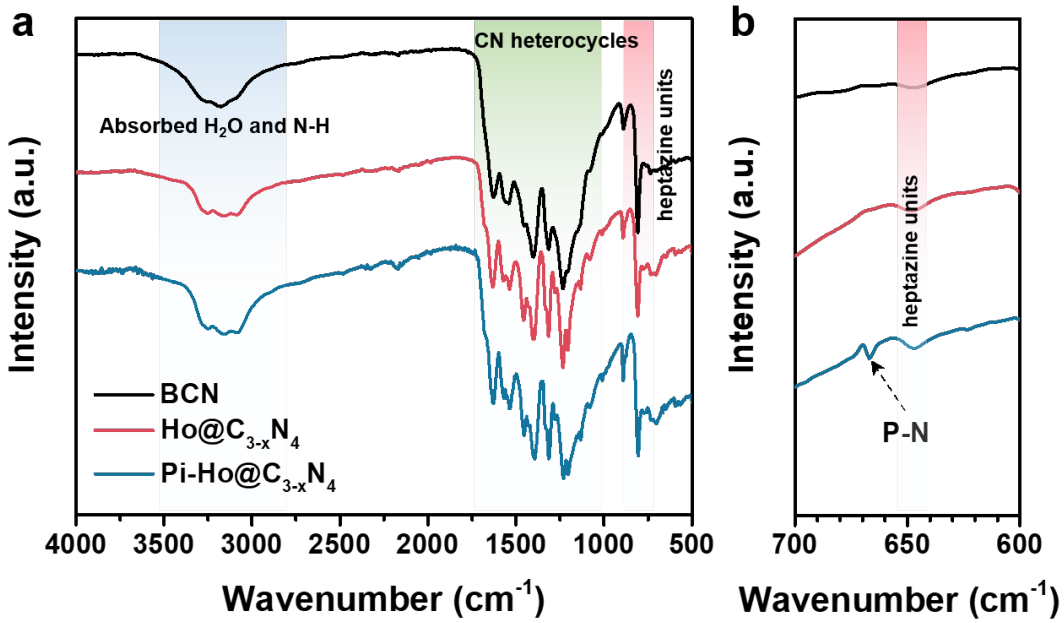

Fig. S6 FTIR profiles of BCN, Ho@$C_{3-x}N_4$ and Pi-Ho@$C_{3-x}N_4$, respectively.

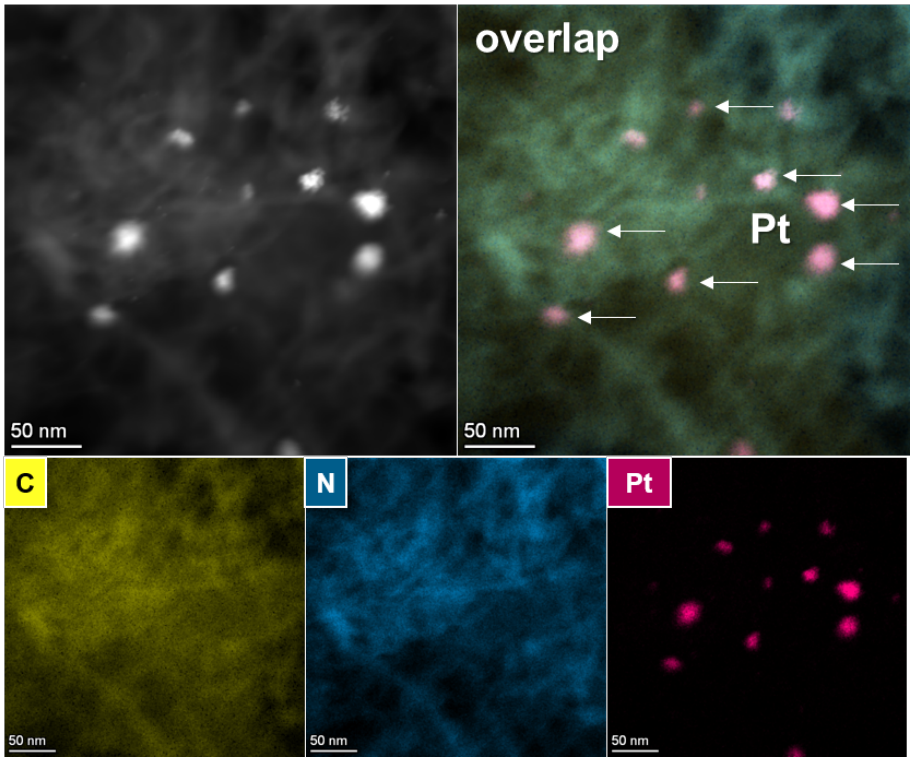

Fig. S7 Morphological study and EDX-mapping of co-catalyst (Pt) on the Pi-Ho@$C_{3-x}N_4$ surface.

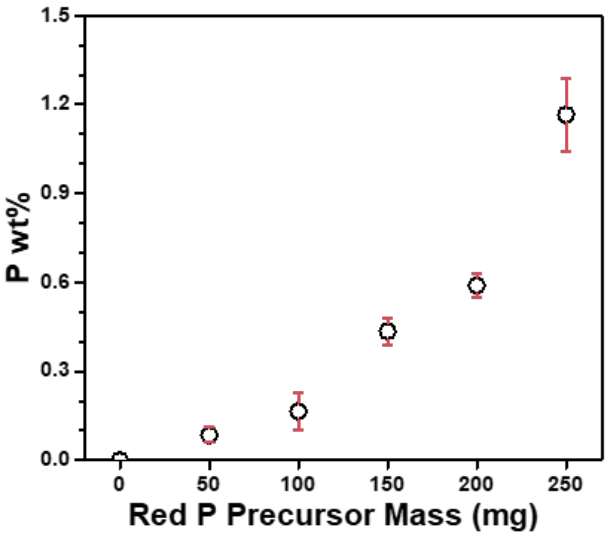

Fig. S8 P weight percent in each sample from EDX statistics.

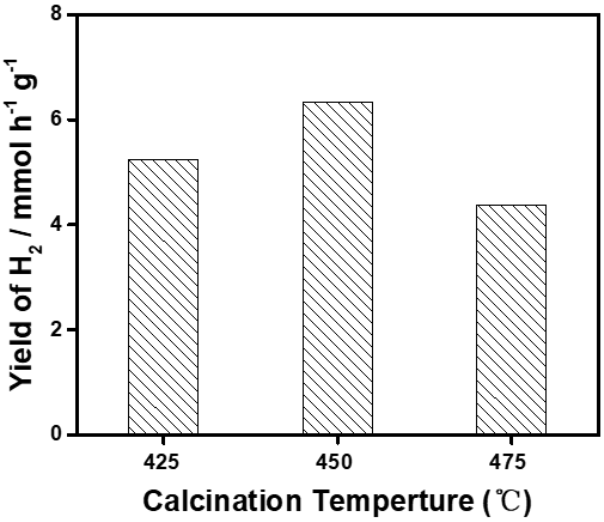

Fig. S9 Comparison of photocatalytic H_2 production activity using synthesized Pi-Ho@$C_{3-x}N_4$ catalysts with different calcination temperatures.

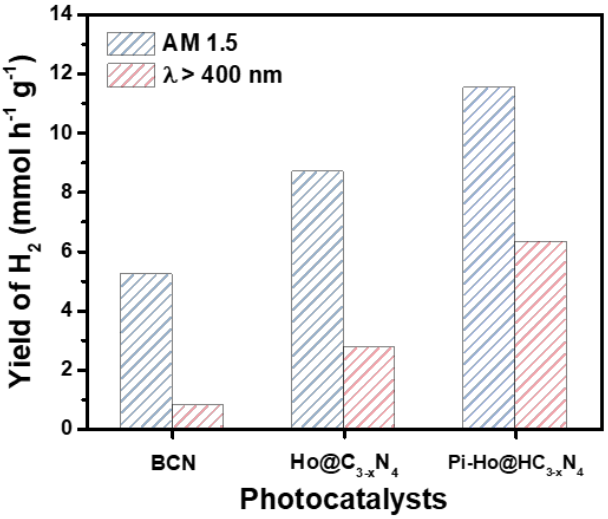

Fig. S10 Comparison of photocatalytic H_2 production activity of BCN, Ho@$C_{3-x}N_4$ and Pi-Ho@$C_{3-x}N_4$ under visible-light and simulated sunlight irradiation, respectively.

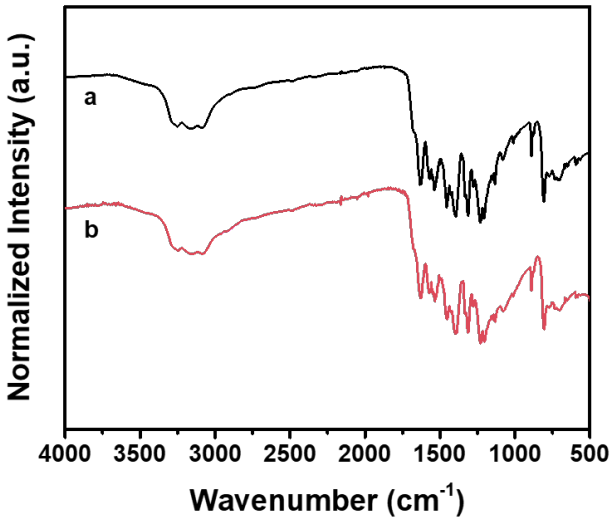

Fig. S11 FTIR profiles of Pi-Ho@$C_{3-x}N_4$ sample: before (a) and after (b) cyclic runs of photocatalytic H_2 production reaction.

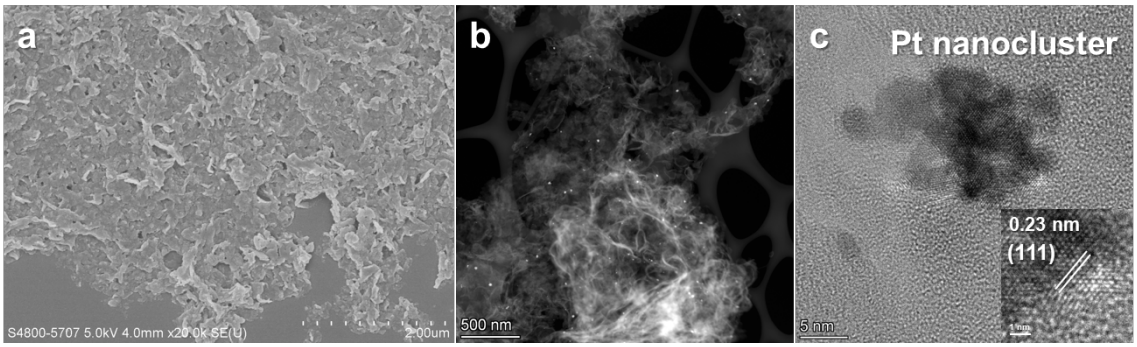

Fig. S12 (a) SEM and (b) STEM image of the Pi-Ho@$C_{3-x}N_4$ sample after cyclic runs of photocatalytic H_2 production reaction; (c) high-resolution STEM image of Pt nanoclusters on Pi-Ho@$C_{3-x}N_4$ surface.

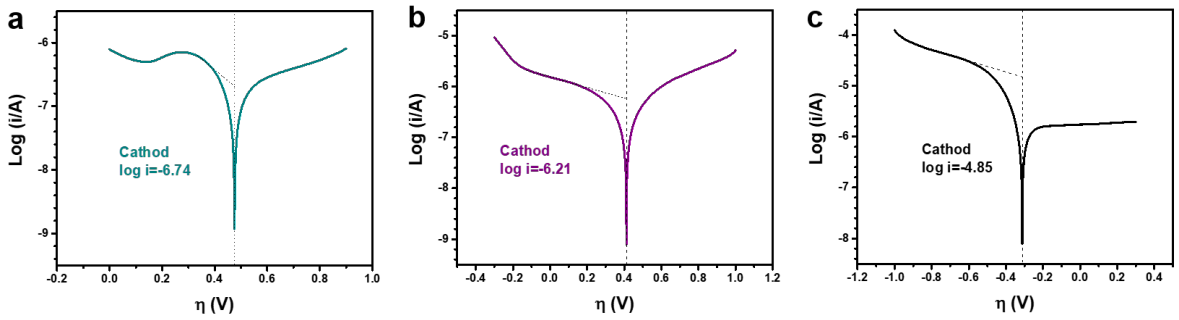

Fig. S13 Tafel plot of (a) BCN, (b) Ho@$C_{3-x}N_4$ and (c) Pi-Ho@$C_{3-x}N_4$.

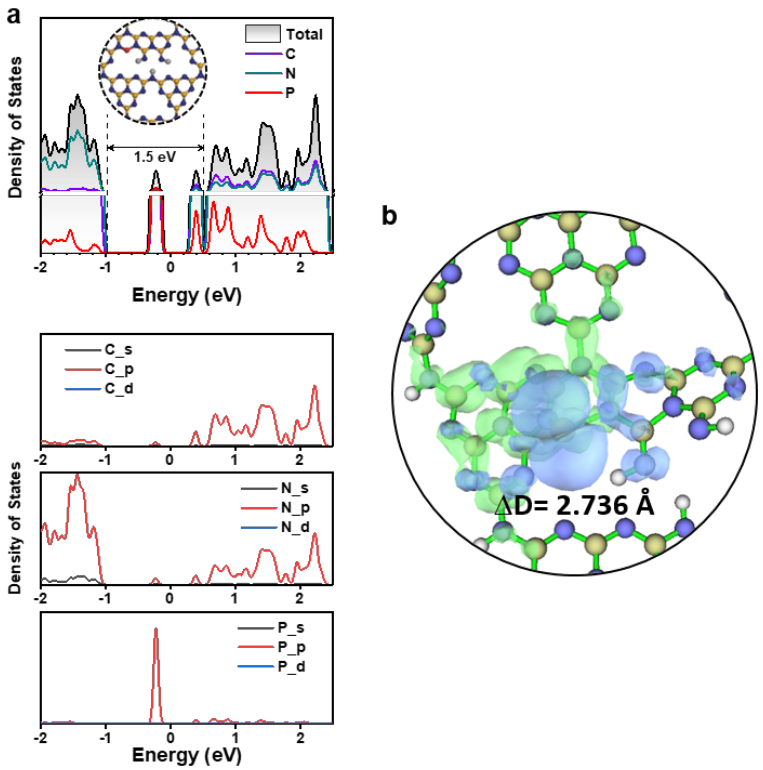

Fig. S14 (a) Calculated density of states (DOS) and (b) Charge density difference of the Pi-Ho@$C_{3-x}N_4$ during the S_0-S_1 transition, calculated using the B3LYP functional with the 6-31G basis set; the green and blue meshes represent the electrons and the holes during the S_0-S_1 transition, respectively.

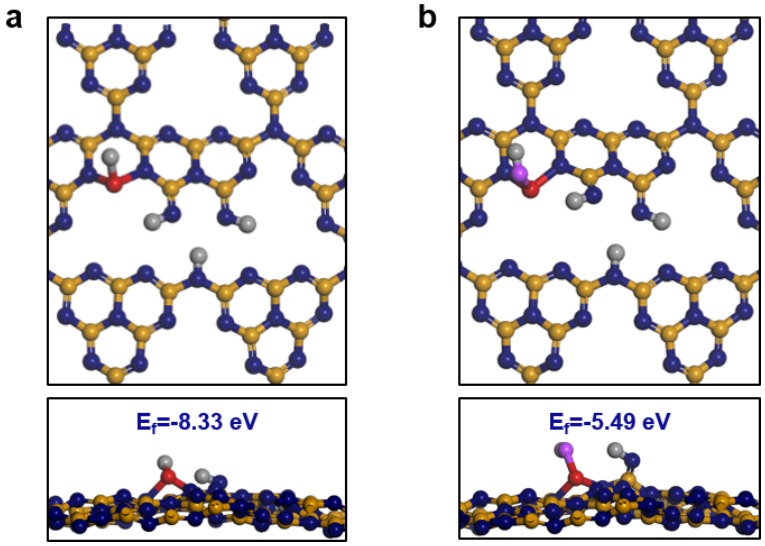

Fig. S15 Simulate the formation energy of the Pi-Ho@$C_{3-x}N_4$ with (a) proton and (b) hydroxy at the interstitial phosphorus-site.

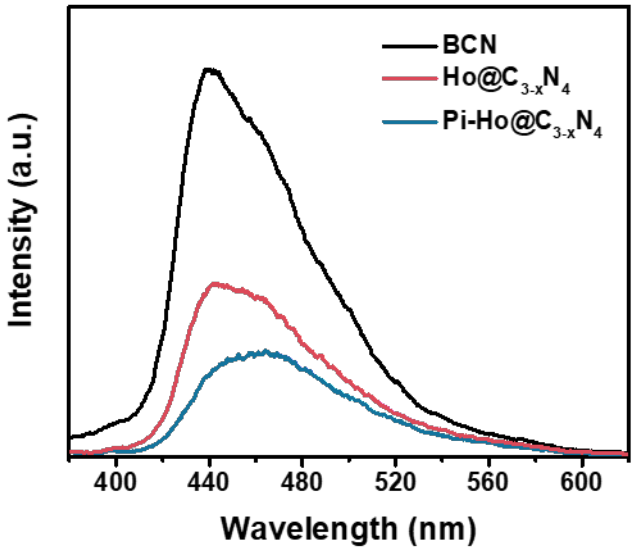

Fig. S16 Steady-state photoluminescence (PL) emission in the inert medium (acetonitrile) under 355 nm laser flash.

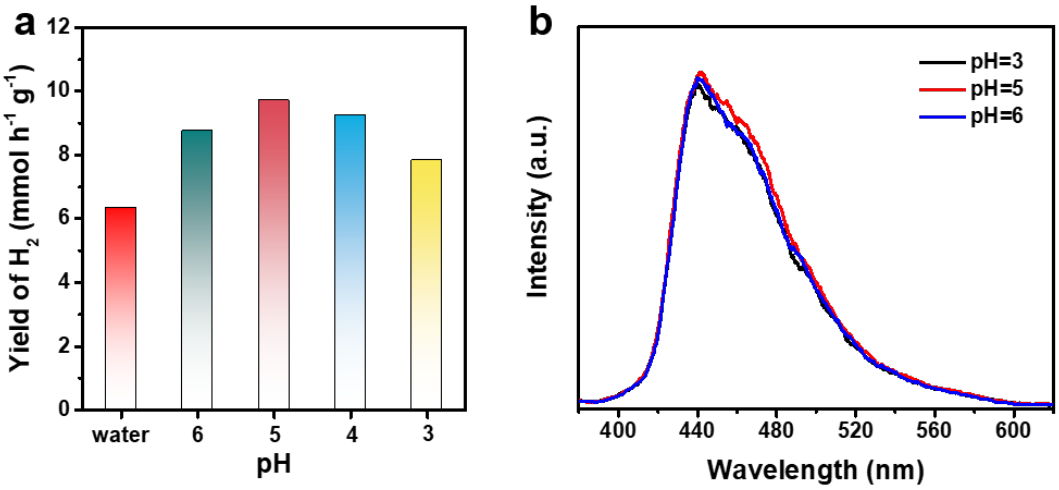

Fig. S17 (a) Comparison of H_2 evolution rates of the Pi-Ho@$C_{3-x}N_4$ photocatalyst in different pH solution; (b) the corresponding steady-state photoluminescence (PL) emission under 355 nm laser flash.

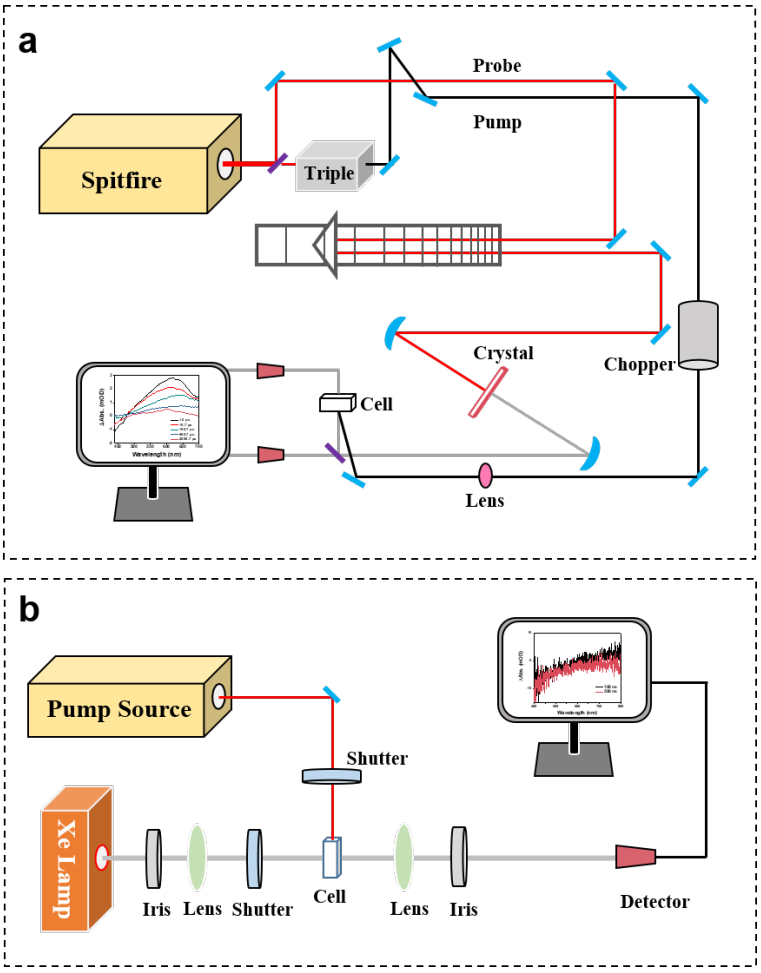

Fig. S18 Schematic illustration of (a) fs-TAS and (b) ns-TAS setup.

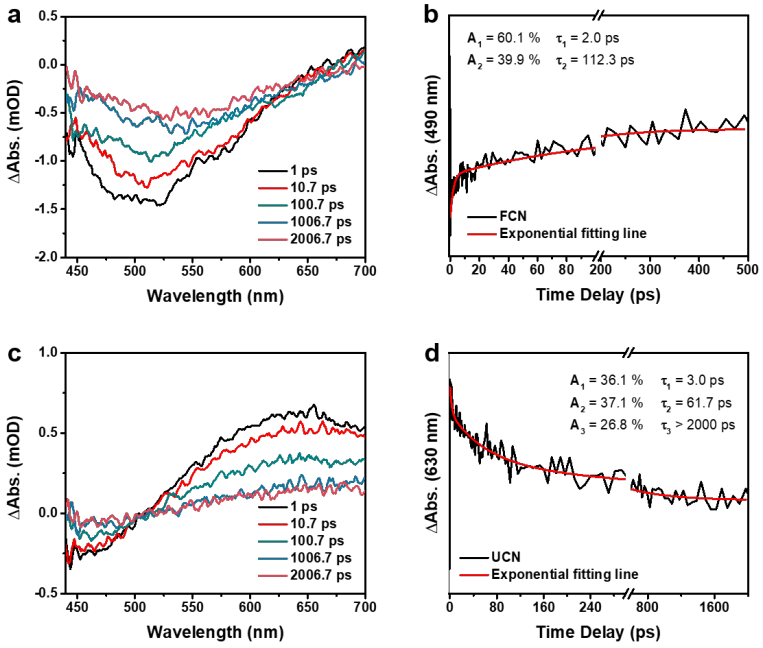

Fig. S19 fs-TAS and kinetics decay process of (a, b) BCN and (c, d) FCN in water.

As a reference, the fs-TAS of FCN and UCN were carried out to determine the kinetic decay process. Compared to the BCN sample, the FCN also shows a broad negative absorption feature from 450 to 650 nm due to the simulate emissions. The shorter lifetime of τ_1 (2.0 ps) and τ_2 (112.3 ps) and the positive absorption in 650-700 nm area demonstrated the enhanced separation of the charge carriers. For UCN, three-time constants with 3.0 ps (τ_1), 61.7 ps (τ_2) and > 2 ns (τ_3) can be assigned to electron-hole recombination, hole trapping and deep electron trapping processes, respectively.

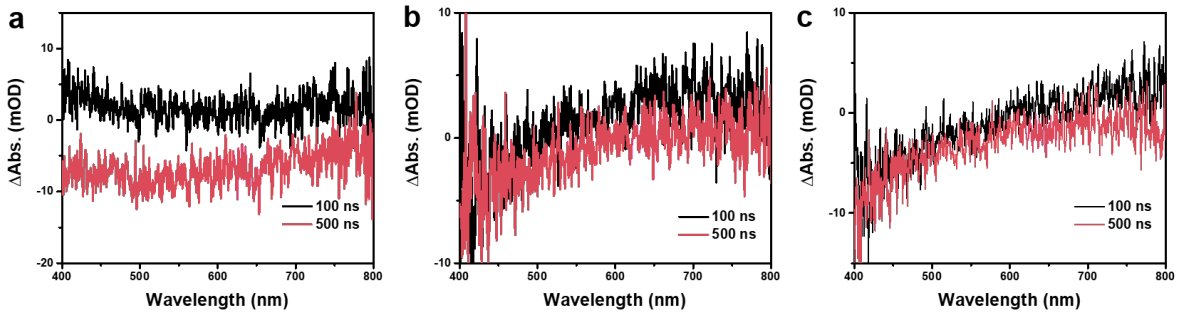

Fig. S20 ns-TAS of (a) BCN, (b) Ho@$C_{3-x}N_4$ and (c) Pi-Ho@$C_{3-x}N_4$.

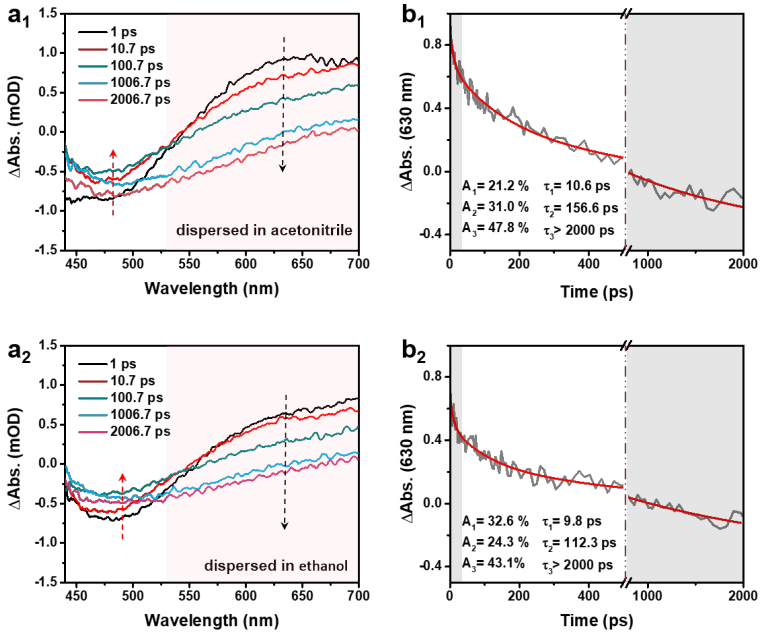

Fig. S21 (a) fs-TAS, and (b) kinetics decay process of the Pi-Ho@$C_{3-x}N_4$ sample in inert solvents: (a_1-b_1) acetonitrile and (a_2-b_2) ethanol.

Table S1. Photocatalytic H_2 production performance of the conventional P-doped g-C_3N_4 photocatalysts (from 2015 to 2022).

Sample	Co-cat.	Reactant Solution	Light	Photoctivity	Year	Ref.
P-doped g-C_3N_4	1 wt% Pt	20 vol% TEOA	λ > 400 nm	1596 μmol h^{-1} g^{-1}	2015	[7]
P-doped g-C_3N_4	1 wt% Pt	20 vol% MeOH	λ > 420 nm	67 μmol h^{-1} (670 μmol h^{-1} g^{-1})	2016	[8]
P-doped g-C_3N_4	1 wt% Pt	20 vol% MeOH	λ > 420 nm	57 μmol h^{-1} (570 μmol h^{-1} g^{-1})	2017	[9]
P-doped g-C_3N_4	3 wt% Pt	10 vol% TEOA	λ > 400 nm	256.4 μmol h^{-1} (5125 μmol h^{-1} g^{-1})	2018	[10]
P-doped g-C_3N_4	1 wt% Pt	10 vol% TEOA	λ > 420 nm	941.8 μmol h^{-1} g^{-1}	2018	[11]
P-doped g-C_3N_4	3 wt% Pt	10 vol% TEOA	λ ≥ 420 nm	2020 μmol h^{-1} g^{-1}	2019	[12]
P,Mo-doped g-C_3N_4	eosin Y (sensitizer)	5 vol% TEOA	λ ≥ 420 nm	118 μmol h^{-1} g^{-1}	2019	[13]
P-doped g-C_3N_4	3 wt% Pt	10 vol% TEOA	λ > 420 nm	171.6 μmol h^{-1} (5720 μmol h^{-1} g^{-1})	2020	[14]
P-doped g-C_3N_4	2 wt% Pt	20 vol% TEOA	λ > 420 nm	2814 μmol h^{-1} g^{-1}	2021	[15]
P-doped g-C_3N_4	MoP	20 vol% TEOA	300 W Xenon-lamp	4917.83 μmol h^{-1} g^{-1}	2022	[16]
Pi-Ho@$C_{3-x}N_4$	3 wt% Pt	10 vol% TEOA	λ > 400 nm	6323 μmol h^{-1} g^{-1}	2022	This work

Table S2. Photocatalytic H_2 production performance of other heteroatom-doped g-C_3N_4 photocatalysts (from 2012 to 2022).

Sample	Co-cat.	Reactant Solution	Light	Photoctivity	Year	Ref.
O-doped g-C_3N_4	1.2 wt% Pt	10 vol% TEOA	$\lambda < 420$ nm	37.5 μmol h^{-1} (375 μmol h^{-1} g^{-1})	2012	[17]
S-doped g-C_3N_4	3 wt% Pt	15 vol% MeOH	$\lambda > 420$ nm	136 μmol h^{-1} g^{-1}	2012	[18]
I-doped g-C_3N_4	3 wt% Pt	10 vol% TEOA	$\lambda > 420$ nm	38 umol h^{-1} (760 μmol h^{-1} g^{-1})	2014	[19]
I-doped g-C_3N_4	3 wt% Pt	10 vol% TEOA	$\lambda > 420$ nm	44.5 μmol h^{-1} (890 μmol h^{-1} g^{-1})	2015	[20]
N-doped g-C_3N_4	3 wt% Pt	10 vol% TEOA	$\lambda > 420$ nm	64 μmol h^{-1} (1280 μmol h^{-1} g^{-1})	2016	[21]
Br-doped g-C_3N_4	3 wt% Pt	10 vol% TEOA	$\lambda \geq 420$ nm	45 μmol h^{-1} (900 μmol h^{-1} g^{-1})	2016	[22]
Co-doped g-C_3N_4	3 wt% Pt	10 vol% TEOA	$\lambda > 420$ nm	28 μmol h^{-1} g^{-1}	2017	[23]
O-doped g-C_3N_4	3 wt% Pt	15 vol% TEOA	$\lambda > 420$ nm	732 μmol h^{-1} g^{-1}	2018	[24]
S-doped g-C_3N_4	5 wt% Ni	20 vol% TEOA	$\lambda > 420$ nm	2021.3 μmol h^{-1} g^{-1}	2018	[25]
B,S-doped g-C_3N_4	1 wt% Pt	10 vol% TEOA	$\lambda \geq 420$ nm	53.2 μmol h^{-1} (2660 μmol h^{-1} g^{-1})	2018	[26]
C-doped g-C_3N_4	0.5 wt% Pt	15 vol% TEOA	$\lambda > 420$ nm	25.0 μmol h^{-1} (2500 μmol h^{-1} g^{-1})	2019	[27]
S-doped g-C_3N_4/$BiPO_4$	3 wt% Pt	17 vol% TEOA	$\lambda > 420$ nm	11.7 μmol h^{-1} (1170 μmol h^{-1} g^{-1})	2020	[28]
O-doped g-C_3N_4	2 wt% Pt	10 vol% TEOA	$\lambda > 420$ nm	73.84 μmol h^{-1} (3692 μmol h^{-1} g^{-1})	2021	[29]
O-doped g-C_3N_4	3 wt% Pt	20 vol% TEOA	$\lambda > 420$ nm	395.96 μmol h^{-1} g^{-1}	2021	[30]
S-doped g-C_3N_4	19.3 wt% N-doped MoS_2	10 vol% TEOA	300 W Xenon-lamp	658.5 μmol h^{-1} g^{-1}	2021	[31]
Pi-Ho@$C_{3-x}N_4$	3 wt% Pt	10 vol% TEOA	$\lambda > 400$ nm	6323 μmol h^{-1} g^{-1}	2022	This work

Table S3. Exponential function fitted parameters of fs-TAS.

Sample	Probe at 630 nm (ESA)						Probe at 460 nm (SE)			
	A_1 [%]	τ_1 [ps]	A_2 [%]	τ_2 [ps]	A_3 [%]	τ_3 [ps]	A_1 [%]	τ_1 [fs]	A_2 [%]	τ_2 [ps]
BCN	-	-	-	-	-	-	82.1	550	17.9	25.9
Ho@$C_{3-x}N_4$	46.5	6.0	39.8	189.9	13.7	> 2000	94.2	222	5.8	17.2
Pi-Ho@$C_{3-x}N_4$	48.9	17.9	45.6	405.5	5.5	> 2000	98.3	< 150	1.7	0.5

Table S4. Comparison of exponential function fitted parameters of ns-TAS.

Sample	A [%]	τ [ns]
BCN	100	110.5
Ho@$C_{3-x}N_4$	100	4.9
Pi-Ho@$C_{3-x}N_4$	100	4.6

References

[1] P. Niu, L. Zhang, G. Liu, H.-M. Cheng, *Adv. Funct. Mater.* **2012**, *22*, 4763-4770.

[2] Z. Lian, Y. Kobayashi, J. J. M. Vequizo, C. S. K. Ranasinghe, A. Yamakata, T. Nagai, K. Kimoto, K. Kobayashi, K. Tanaka, T. Teranishi, M. Sakamoto, *Nat. Sustain.* **2022,** https://doi.org/10.1038/s41893-022-00975-9.

[3] M. S. Kodaimati, S. Lian, G. C. Schatz, E. A. Weiss, *PNAS* **2018**, *115*, 8290-8295.

[4] P. E. Blöchl, *Phys. Rev. B* **1994**, *50*, 17953-17979.

[5] J. P. Perdew, K. Burke, M. Ernzerhof, *Phys. Rev. Lett.* **1996**, *77*, 3865-3868.

[6] X. Li, J. Hu, T. Yang, X. Yang, J. Qu, C. M. Li, *Nano Energy* **2022**, *92*, 106714.

[7] J. Ran, T. Y. Ma, G. Gao, X.-W. Du, S. Z. Qiao, *Energy Environ. Sci.* **2015**, *8*, 3708-3717.

[8] S. Guo, Z. Deng, M. Li, B. Jiang, C. Tian, Q. Pan, H. Fu, *Angew. Chem. Int. Ed.* **2016**, *55*, 1830-1834.

[9] S. Guo, Y. Tang, Y. Xie, C. Tian, Q. Feng, W. Zhou, B. Jiang, *Appl. Catal. B* **2017**, *218*, 664-671.

[10] H. Yang, Y. Zhou, Y. Wang, S. Hu, B. Wang, Q. Liao, H. Li, J. Bao, G. Ge, S. Jia, *J. Mater. Chem. A* **2018**, *6*, 16485-16494.

[11] J. Feng, D. Zhang, H. Zhou, M. Pi, X. Wang, S. Chen, *ACS Sustainable Chem. Eng.* **2018**, *6*, 6342-6349.

[12] M. Wu, J. Zhang, B.-b. He, H.-w. Wang, R. Wang, Y.-s. Gong, *Appl. Catal. B* **2019**, *241*, 159-166.

[13] D. Chen, J. Liu, Z. Jia, J. Fang, F. Yang, Y. Tang, K. Wu, Z. Liu, Z. Fang, *J. Hazard. Mater.* **2019**, *361*, 294-304.

[14] Y. Zhu, J. Li, J. Cao, C. Lv, G. Huang, G. Zhang, Y. Xu, S. Zhang, P. Meng, T. Zhan, D. Yang, *APL Mater.* **2020**, *8*, 041108.

[15] S. Lv, Y. H. Ng, R. Zhu, S. Li, C. Wu, Y. Liu, Y. Zhang, L. Jing, J. Deng, H. Dai, *Appl. Catal. B* **2021**, *297*, 120438.

[16] X. Wang, X. Wang, W. Tian, A. Meng, Z. Li, S. Li, L. Wang, G. Li, *Appl. Catal. B* **2022**, *303*, 120933.

[17] J. Li, B. Shen, Z. Hong, B. Lin, B. Gao, Y. Chen, *Chem. Commun.* **2012**, *48*, 12017-12019.

[18] J. Hong, X. Xia, Y. Wang, R. Xu, *J. Mater. Chem.* **2012**, *22*, 15006-15012.

[19] G. Zhang, M. Zhang, X. Ye, X. Qiu, S. Lin, X. Wang, *Adv. Mater.* **2014**, *26*, 805-809.

[20] Q. Han, C. Hu, F. Zhao, Z. Zhang, N. Chen, L. Qu, *J. Mater. Chem. A* **2015**, *3*, 4612-4619.

[21] Y. Zhou, L. Zhang, W. Huang, Q. Kong, X. Fan, M. Wang, J. Shi, *Carbon* **2016**, *99*, 111-117.

[22] Z.-A. Lan, G. Zhang, X. Wang, *Appl. Catal. B* **2016**, *192*, 116-125.

[23] P.-W. Chen, K. Li, Y.-X. Yu, W.-D. Zhang, *Appl. Surf. Sci.* **2017**, *392*, 608-615.

[24] Y. Zeng, X. Liu, C. Liu, L. Wang, Y. Xia, S. Zhang, S. Luo, Y. Pei, *Appl. Catal. B* **2018**, *224*, 1-9.

[25] C. Sun, H. Zhang, H. Liu, X. Zheng, W. Zou, L. Dong, L. Qi, *Appl. Catal. B* **2018**, *235*, 66-74.
[26] P. Babu, S. Mohanty, B. Naik, K. Parida, *ACS Appl. Energy Mater.* **2018**, *1*, 5936-5947.
[27] J. Li, D. Wu, J. Iocozzia, H. Du, X. Liu, Y. Yuan, W. Zhou, Z. Li, Z. Xue, Z. Lin, *Angew. Chem. Int. Ed.* **2019**, *58*, 1985-1989.
[28] D. Long, Z. Chen, X. Rao, Y. Zhang, *ACS Appl. Energy Mater.* **2020**, *3*, 5024-5030.
[29] Y. Zhang, Z. Chen, J. Li, Z. Lu, X. Wang, *J. Energy Chem.* **2021**, *54*, 36-44.
[30] Y. Jiang, Z. Sun, C. Tang, Y. Zhou, L. Zeng, L. Huang, *Appl. Catal. B* **2019**, *240*, 30-38.
[31] Y. Chen, F. Su, H. Xie, R. Wang, C. Ding, J. Huang, Y. Xu, L. Ye, *Chem. Eng. J.* **2021**, *404*, 126498.